



# Gradient design of bio-inspired nacre-like composites for improved impact resistance

Zhiqian Wei<sup>a,b</sup>, Xianghong Xu<sup>a,\*</sup>

<sup>a</sup> LNM, Institute of Mechanics, Chinese Academy of Sciences, Beijing, 100190, China

<sup>b</sup> School of Engineering Sciences, University of Chinese Academy of Sciences, Beijing, 100049, China

## ARTICLE INFO

### Keywords:

Nacre-like structure  
Gradient design  
Impact resistance

## ABSTRACT

A novel brick-mud structure was proposed by introducing cell size gradient design into the nacre-like brick-mud microstructure. The gradient brick-mud structure samples were successfully prepared with the 3D printing technology. It was found through a pendulum impact test that the energy absorption of the gradient structure was higher than that of the uniform structure. With the gradient increase in the cell size, the energy absorption increased and could reach up to 4 times that of the uniform structure. A finite element simulation method was used to explore the energy absorption improvement mechanism of the gradient structure. The results showed that compared with the uniform structure, the gradient structure can achieve a much better stress distribution, which leads to greater bending deformation before fracture, thus improving strain energy storage. Moreover, the strain energy stored in the stiff material was about 2 times that of the soft material, and the strain energy stored in the interlayer soft material was 10 times that of the intralayer soft material.

## 1. Introduction

After hundreds of millions of years of selection and evolution in nature, the living beings continuously optimized themselves and improved their structures and performances [1,2], where the perfect structures of the bio-materials enlighten the design of artificial materials [3,4]. The nacre, known as stiff and tough, has a typical brick-mud microstructure [5,6]. Since the mismatching of physical properties of a soft interface and a stiff interface is perfectly solved, stress concentration can be effectively relieved, cracks are deflected to a certain degree, and brittle failure is avoided. Therefore, the nacre structure has high strength, high toughness, and enhanced impact resistance [7,8].

Based on the brick-mud structure characteristics of the nacre, Flores-Johnson et al. [9] designed a brick-mud structure composed of five brick-mud structure layers and four soft material layers between the brick-mud layers, and cells of the brick-mud structure layers were squares of the same size. Aluminum alloy AA7075 and epoxy resin were adopted as the stiff and soft materials, respectively. The numerical simulation showed that, under the impact of a bullet of velocity of 900 m/s, the brick-mud structure had a larger plastic deformation area, and the energy absorption was increased by 44%, compared with the structure with a single stiff material which has smaller plastic

deformation area and brittle fracture. Tran et al. [10,11] also designed a brick-mud structure composed of five brick-mud structure layers and four soft material layers between the brick-mud layers. The cells of the brick-mud structure layers were Voronoi polygons with similar sizes, aluminum and vinyl ester resin were adopted as the stiff and soft materials, respectively. The numerical simulation showed that under exposure of explosion impact on the structures, the soft material was conducive to the dissipating of the energy of explosive shock waves. Gu et al. [12] prepared a structure composed of only eight tightly connected brick-mud structure layers, and the cells of the brick-mud structure layers were rectangles of the same size. Veromagenta and Tango-BlackPlus were the stiff and soft materials, respectively. The falling weight impact test and the numerical simulation result showed that due to that the brick-mud structure improved the stress distribution and thus effectively avoided stress localization, the overall structure was in a mode of progressive failure, and the energy absorption in the impact process was 30% higher than that of the single stiff material structure.

Further research results have shown that the arrangement way of the brick-mud microstructure has a significant influence on the impact resistance of the structure [13,14]. Gu et al. [12,15] designed a brick-mud structure composed of three brick-mud structure layers and two soft material layers in between by imitating conch shells, where the

\* Corresponding author.

E-mail address: [xhx@lnm.imech.ac.cn](mailto:xhx@lnm.imech.ac.cn) (X. Xu).

<https://doi.org/10.1016/j.compositesb.2021.108830>

Received 3 January 2021; Received in revised form 20 March 2021; Accepted 21 March 2021

Available online 24 March 2021

1359-8368/© 2021 Elsevier Ltd. All rights reserved.

soft materials were arranged in a multistage cross form. Veromagenta and TangoBlackPlus were adopted as the stiff and soft materials, respectively, in the conch shell-like structure. The falling weight impact test results showed that, compared with the nacre-like structure with the same volume fraction of the soft material, the conch shell-like structure had the advantage of increased deflection degree of internal cracks, and thus the crack extension path was longer and the energy absorption was increased by 70%. Jiang et al. [16] imitated mantis shrimp dactyl club [17], and designed a brick-mud structure in which stiff materials followed a spiral spatial distribution. Carbon fibers and epoxy resin were adopted as the stiff and soft materials, respectively. Under falling weight impact, the crack distortion effect occurred; the greater rotation angle between adjacent layers can produce longer crack path along the thickness direction, and thus the energy needed for fracture was increased, showing better impact resistance. By imitating sponge, Jia et al. [13] designed and prepared a layered-bulk brick-mud structure where the soft materials and the stiff materials were interlaced. Vero-white and TangoPlus were adopted as the stiff and soft materials, respectively. The dynamic three-point bending test showed that with the same volume fractions of the soft materials, the energy absorption of the composite structure was increased by 76%, compared with the nacre-like structure. It was due to that the composite structure had both the lower crack driving force of the layered structure and the greater rigidity of the bulk structure, and that the stress distribution was improved. Therefore, cracks deflected towards both sides in the sub-structure of the bulk, and thus effectively avoided catastrophic damage.

In addition, researchers have extensively investigated the influence of the strength of the soft material [18], the inclination angle of the soft material in the brick-mud structure layer [15] and the length-width ratio of the cells [19] on the impact resistance of the nacre-like brick-mud structure. The soft material in the brick-mud structure plays a role of adapting to deformation and improving the stress distribution [20]. Optimization of the soft material can further increase the impact resistance [18,21]. Ni et al. [18] designed a brick-mud structure composed of five brick-mud structure layers inter-spaced with four soft material layers, and the cells of the brick-mud structure layers were Voronoi polygons with similar sizes. Mineral substances and organic matters in natural nacles were adopted as the stiff and soft materials, respectively. It was also assumed that the ratio of shear strength to tensile strength of the soft materials was constantly 1.5. The numerical simulation of falling weight impact test showed that, when the initial speed of the hammer head was 2.5 m/s and the shear strength of the soft material was 1.5 MPa, the failure mode was a delamination mode, and the impact energy was mainly dissipated through layer separation; and when the shear strength of the soft material was increased to 45.0 MPa, a transition failure mode between layering and perforation was presented. Interlayer delamination and intralayer crack propagation jointly dissipated the impact energy so that the energy absorption of the brick-mud structure was increased by 64%. On the basis of the relationship between energy release rate and material fracture toughness, Gu et al. [15] established a theoretical model of local crack propagation in the conch shell-like brick-mud structure. Veromagenta and TangoBlackPlus were adopted as the stiff and soft materials, respectively. It was found that when the inclination angle of the soft material was less than 50°, the cracks would deflect into the soft material; when the inclination angle was greater than 50° and less than 90°, the cracks would deflect into the stiff material; and when the inclination angle was 50°, the cracks would stop extending. Therefore, an optimal deflection angle of the soft material was obtained. Wu et al. [19] prepared a brick-mud structure composed of nine brick-mud structure layers inter-spaced with eight soft material layers with the 3D printing technology. The cells were regular quadrangles, and the VeroWhitePlus and TangoPlus were adopted as the stiff and soft materials, respectively. The dynamic three-point bending test showed that with smaller length-width ratio of the cells, the cracks were likely to extend bypassing the stiff material and along the soft material, and with larger length-width ratio of the cells, the cracks were

likely to directly penetrate through the stiff material. These two extreme conditions were not facilitated for the energy absorption. When the length-width ratio of the cells was increased from 0.5 to an intermediate value 2.0, the energy absorption was increased by 58%. So far, the energy absorption of protective materials has been increased to a high extent by optimizing the brick-mud structure.

Besides the stiff-soft interlaced structure, gradient distribution of the microstructure is another important characteristic in some impact-resistant biomaterials [22,23]. In recent years, the microstructure size gradient distribution has been introduced into the design of porous structures [24,25] and metal materials [26,27]. It is found that the energy absorption performance of the structure under loading can be remarkably improved with the microstructure size gradient design.

In this paper, a nacre-like brick-mud structure with the cell size changing in a gradient mode was proposed. The influence of cell size gradient on the impact resistance of the brick-mud structure and its behavior mechanism were studied by combining pendulum impact test with finite element numerical simulation. Through this study, a new idea was provided for the design of a novel impact-resistant composite structure.

## 2. Gradient Voronoi brick-mud structure

A group of cell cores distributed in a 2D region expands outwards in a circular manner at a constant rate. When any two adjacent cell walls get into contact, the cell walls are controlled to maintain the state of contact without penetration until the expanded polygons fill up this 2D space before the 2D Voronoi polygon structure can be generated. The common edge of any two adjacent Voronoi polygons is the vertical bisector of the line that connects both cell cores [28,29]. The random scatter method for gradient grid division was used to generate gradient Voronoi polygons and a gradient brick-mud structure in a two-dimensional area with a length of  $L$  and a width of  $W$ . Then, a rectangular area having a length of  $l$  and a width of  $w$  and sharing a common  $y$ -direction symmetric axis with the aforesaid two-dimensional area was chosen as the sample for pendulum impact test (Fig. 1(a)).

### 2.1. Gradient Voronoi polygons

As shown in Fig. 1(b), the two-dimensional area  $L \times W$  is divided into  $J$  columns, and a left boundary and a right boundary satisfying a rectangular area  $l \times w$  are located in the first column of grids and the  $J^{\text{th}}$  column of grids, respectively. If  $J$  is an odd number, the central axis of the  $(J+1)/2^{\text{th}}$  column is used as the  $y$ -direction symmetry axes of the two-dimensional area. If  $J$  is an even number, the common side of the  $(J/2)^{\text{th}}$  column and the  $(J/2+1)^{\text{th}}$  column is used as the  $y$ -direction symmetry axes of the two-dimensional area. The  $j^{\text{th}}$  column is equally divided into  $N_j$  ( $j = 1, 2, \dots, J$ ) square grids, and then the grid width is  $w_j = W/N_j$ . With the center  $o_{ij}$  ( $i = 1, 2, \dots, N_j$ ;  $j = 1, 2, \dots, J$ ) of the grid as the center of a circle of radius  $\xi_j = \lambda w_j$  ( $0 \leq \lambda \leq 1$ ), a cell core  $P_{ij}$  is scattered on the circle. The coordinates of the cell core  $P_{ij}$  can be expressed as

$$\begin{cases} x_{ij} = \sum_{t=1}^j w_{t-1} + \frac{w_j}{2} + \xi_j \cos \alpha_{ij} \\ y_{ij} = (j-0.5)w_j + [1 - \text{FIX}(N_j)/N_j]W/2 + \xi_j \sin \alpha_{ij} \end{cases} \quad (1)$$

where  $w_0 = 0$ ;  $\alpha_{ij}$  is the central angle formed by rotating anticlockwise from the positive direction of the  $x$  axis to  $o_{ij}A_{ij}$ , and a random number between  $[0, 2\pi]$  is taken; FIX is downward rounding function;  $\lambda$  represents the order degree of point scattering, the smaller the value is, the more ordered the distribution of the Voronoi polygon cores are. Here,  $\lambda = 0.1$ .

Fig. 1(c) shows the generated gradient Voronoi polygons. Most of the cells located at the boundary are incomplete Voronoi polygons, which are excluded for statistical calculation of the sizes of the cells. The

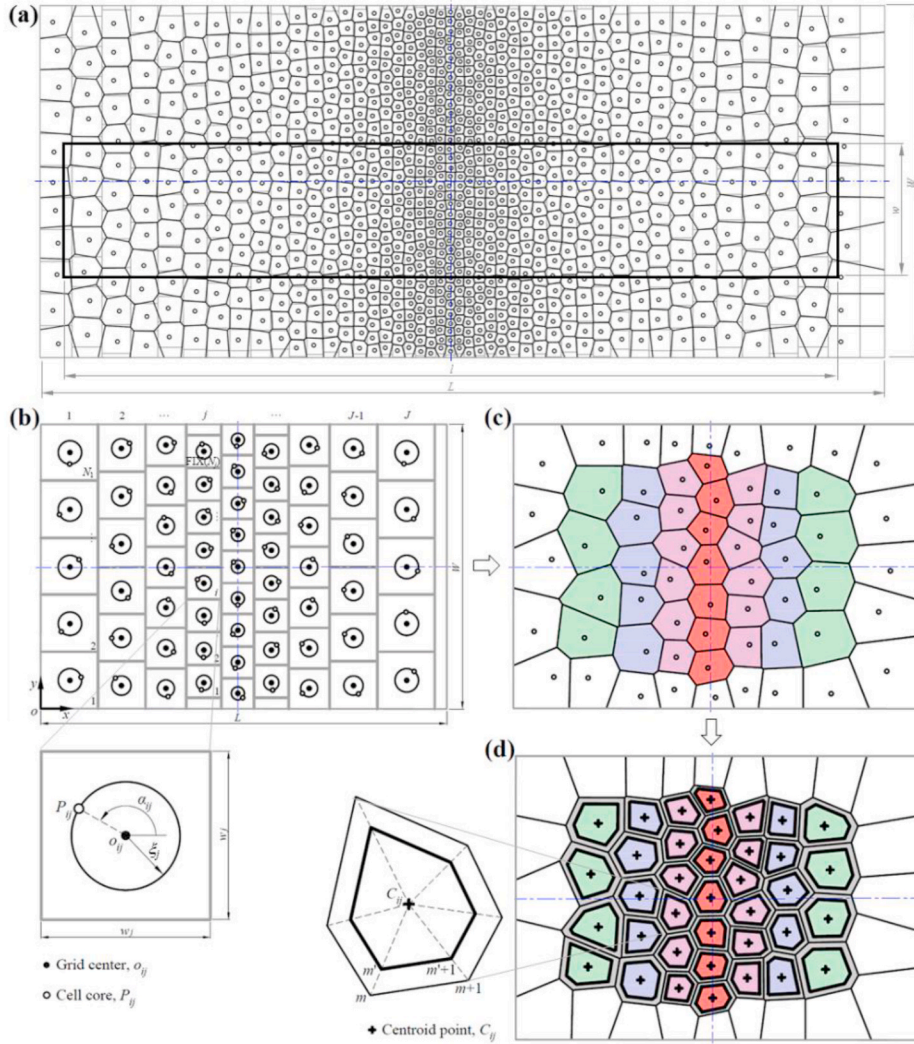


**Fig. 1.** Generation diagram of brick-mud structure. (a) Model size; (b) Random scatter method for gradient grid division; (c) Gradient Voronoi polygons; (d) Brick-mud structure.

average size  $r_j$  of the cells in  $j$ th column can be defined as

$$r_j = \sqrt{\frac{\sum_{i=2}^{\text{FIX}(N_j)-1} A_{ij}}{[\pi(\text{FIX}(N_j) - 2)]}}, \quad j = 2, 3, \dots, J-1 \quad (2)$$

where  $A_{ij}$  is the area of the Voronoi polygon located in the  $i$ th row and the  $j$ th column. By controlling the number  $N_j$  of cell cores, the cell sizes can be in linear gradient distribution along the  $x$  direction. Then the cell size gradient can be expressed as

$$k = \frac{r_2 - r_{\text{FIX}((J+1)/2)}}{l/2} \quad (3)$$

## 2.2. Brick-mud structure model

As shown in the Fig. 1(d), the Voronoi polygon located in the  $i$ th row and the  $j$ th column is an  $M$  polygon, the coordinates of the  $m$ th ( $m = 1, 2, \dots, M$ ) vertex are  $(x_m, y_m)$ , and the coordinates  $(x_{Cij}, y_{Cij})$  of the centroid  $C_{ij}$  can be expressed as [30]

$$\begin{cases} x_{C_{ij}} = \frac{1}{6A_{ij}} \sum_{m=1}^M (x_m + x_{m+1})(x_m y_{m+1} - x_{m+1} y_m) \\ y_{C_{ij}} = \frac{1}{6A_{ij}} \sum_{m=1}^M (y_m + y_{m+1})(x_m y_{m+1} - x_{m+1} y_m) \end{cases} \quad (4)$$

where  $x_{M+1} = x_1$ ,  $y_{M+1} = y_1$ ;  $A_{ij}$  can be calculated according to the vertex coordinates

$$A_{ij} = \frac{1}{2} \sum_{m=1}^M (x_m y_{m+1} - x_{m+1} y_m) \quad (5)$$

With the centroid  $C_{ij}$  of the Voronoi polygon as a base point, the Voronoi polygon is shrunk, and the scaling factors for all polygons are the same. Then ratio of the area  $A_{ij}$  of the original polygon to the shrunken area  $A'_{ij}$  is a constant

$$V_f = \frac{A'_{ij}}{A_{ij}} \quad (6)$$

According to the geometric similarity, the following equation can be obtained,



$$\frac{A'_{ij}}{A_{ij}} = \frac{(x_{C_{ij}} - x_{m'})^2}{(x_{C_{ij}} - x_m)^2} = \frac{(y_{C_{ij}} - y_{m'})^2}{(y_{C_{ij}} - y_m)^2} \quad (7)$$

where  $(x_m, y_m)$  ( $m = 1, 2, \dots, M$ ) is the coordinates of the  $m$ th vertex of the newly generated Voronoi polygon. According to Equations (6) and (7),

$$\begin{cases} x_{m'} = x_{C_{ij}} - \sqrt{(1 - V_f)}(x_{C_{ij}} - x_m) \\ y_{m'} = y_{C_{ij}} - \sqrt{(1 - V_f)}(y_{C_{ij}} - y_m) \end{cases} \quad (8)$$

During modeling, the volume fraction  $V_f$  of the stiff material in the brick-mud structure layer is given, the vertex coordinates of the new Voronoi polygon can be obtained through Equation (8), and the vertex coordinates are sequentially connected to generate a shrunken Voronoi polygon. During assignment of material parameters, the newly generated polygon is internally provided with a stiff material, and the gray area between the polygons is provided with a soft material. Then a brick-mud structure formed by the soft material and the stiff material is generated (Fig. 1(d)).

### 2.3. Design of quasi-linear gradient brick-mud structure

The size of the brick-mud sample is  $55 \text{ mm} \times 10 \text{ mm} \times 10 \text{ mm}$  (Fig. 2(a)). Along the thickness direction of the sample, there are 11 layers in total, including 6 brick-mud structure layers and 5 soft material layers. The volume fractions of the soft material and the stiff material of the sample are 23% and 77%, respectively. The thickness of the soft material layer and brick-mud structure layer are  $0.1250 \text{ mm}$  and  $1.5625 \text{ mm}$ , respectively. The volume fraction  $V_f$  of the stiff material in the brick-mud structure layer is 90%.

When the brick-mud structure layer is modeled, take  $L = 60 \text{ mm}$ ,  $W = 25 \text{ mm}$ ,  $l = 55 \text{ mm}$ , and  $w = 10 \text{ mm}$ . Moreover, the odd layers 1st, 3rd and 5th are completely the same, and  $J$  is an odd number correspondingly. The even layers 2nd, 4th and 6th are also completely the same, and  $J$  is an odd number correspondingly.  $N_j$  is constructed as

$$N_j = 0.25j^n + N_1, \quad j = 2, 3, \dots, \text{FIX}((J + 1) / 2) \quad (9)$$

where,  $N_1 = 11$ . When  $n = 0, 1.40, 1.55$  and  $1.63$ , the cell size  $r_i$  is distributed along the lengthwise direction as shown in Fig. 3(a), where the abscissa represents the average distance from the centroid of each column of cells to the symmetry axis of the sample. The cell size gradients are  $k = 0, 0.0237, 0.0301$  and  $0.0353$ , corresponding to a brick-mud structure model of one uniform and three different cell size gradients (Fig. 3(b)). In order to avoid problems in finite element simulation calculation such as misconvergence or grid distortion and negative volume, the extremely short sides in the structure are deleted, vertexes corresponding to the Voronoi polygons near the extremely short sides are merged to the midpoints of the short sides, small triangles near the boundary are deleted, and the sides corresponding to the Voronoi polygons near the small triangles are extended to intersect [31].

## 3. Experiment and finite element simulation

### 3.1. Sample preparation and pendulum impact test

Brick-mud samples were prepared with the Connex Object 260 printing, where Verowhite and TangoPlus were adopted as the stiff and soft materials, respectively (Fig. 2(b)). After printing was completed, the samples were placed for 24 h at the room temperature. Then the supporting materials on the surface of the samples were removed, and the samples were placed for three days for complete curing. An Instron 750 MPX type pendulum impact testing machine was used for carrying out impact experiments. The span was  $40 \text{ mm}$ . The initial position of the hammer head was adjusted, so that the impact velocity was  $1.1344 \text{ m/s}$ . The energy accuracy was  $0.01 \text{ J}$ . The mass of the hammer head was  $54.376 \text{ kg}$ . The curvature radius of the tip end of the hammer head was  $2 \text{ mm}$ , and the curvature radius of the tip end of a support was  $1 \text{ mm}$ . Three tests were repeated for each structure.

### 3.2. Material parameters

According to the ASTM D638 standard and ASTM D412 standard, respectively, dumbbell-shaped tensile samples of stiff Verowhite and soft Tangoplus were prepared with the 3D printing technology. Single axial tensile tests were performed using Instron 5848 MicroTester. The loading speed of the testing machine was set as  $500 \text{ mm/min}$ , and the

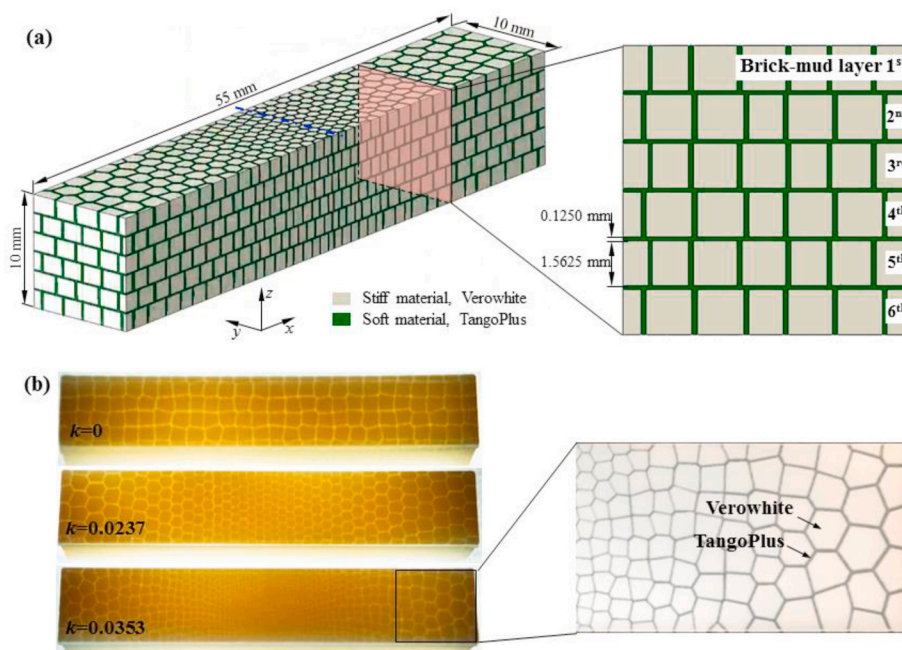


Fig. 2. Brick-mud samples and pendulum impact test. (a) 3D model of brick-mud structure; (b) Brick-mud samples.



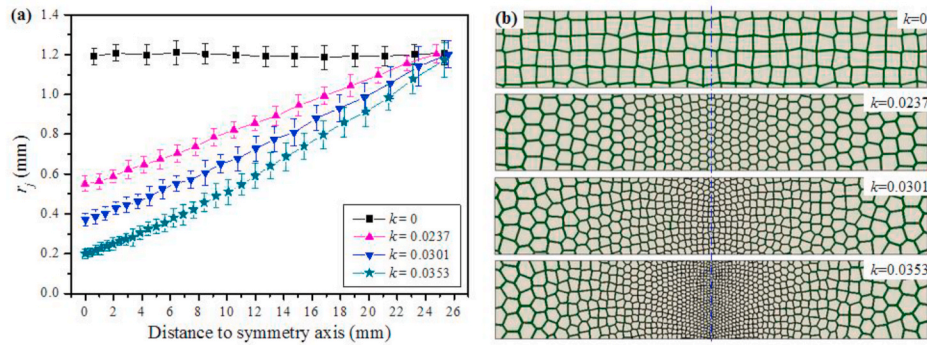


Fig. 3. 1st, 3rd and 5th brick-mud structure layers: (a) Distribution of cell size  $r_j$ ; (b) Brick-mud structures.

constitutive curves of the Verowhite (Fig. 4(a)) and TangoPlus (Fig. 4(b)) at low strain rates were measured. Previous studies [15] have shown that Verowhite-like stiff materials do not have a significant strain rate effect, while TangoPlus-like stiff materials has an obvious strain rate effect at high strain rate. For Verowhite, it was assumed that the constitutive curve at medium strain rate was the same as that obtained at the low strain rate obtained through experiments. The elastic modulus, Poisson ratio and density of Verowhite were 3.00 GPa, 0.30, 1200 kg/m<sup>3</sup>, respectively. For TangoPlus, the constitutive curve at medium strain rate can be obtained as follows. The stress value and the strain rate of TangoBlackPlus, of which performance parameters are approximate to those of the TangoPlus material [32], under the same strain were in positive correlation. That is, when the strain is 0.2, the stress of TangoBlackPlus is almost constantly about 0.2 MPa at low strain rate, but is about 16 MPa at high strain rate. Moreover, the strength and the logarithm of the strain rate of some polymer materials are in a linear relation [33,34]. Therefore, 8.1 MPa, the average value of stresses at low and high strain rates, was assumed as the stress at medium strain rate. Based on the constitutive curve strain of TangoPlus at the low strain rate obtained through experiments, the stress at each point was magnified by 40.5 times, and then the constitutive curve at the assumed medium strain rate was obtained. Then, the assumed constitutive curve was fitted through the high polymer material parameter calibration software MCalification to obtain Arruda-Boyce-Rubber constitutive model parameters, including the shear modulus, bulk modulus, density and the number of statistical links, which were 12.0 MPa, 10<sup>4</sup> MPa, 1200 kg/m<sup>3</sup>, and 100, respectively.

### 3.3. Finite element simulation

The impact process by pendulum bob was simulated by adopting nonlinear dynamic finite element software LS-DYNA. A specific elastic-plastic constitutive model (\*MAT\_PLASTICITY\_POLYMER) [35] for high polymers in LS-DYNA Material Database was adopted for Verowhite. The failure and deletion of an element was simulated by the first

principal stress failure criterion (\*MAT\_ADD\_EROSION), which indicates that, when the first principal stress of a certain element exceeds the failure stress, the element will be deleted. The rubber constitutive model (\*MAT\_ARRUDA-BOYCE-RUBBER) [35] in LS-DYNA Material Database was used for TangoPlus. The failure and deletion process of the element was simulated by the first principal strain failure criterion (\*MAT\_ADD\_EROSION). Moreover, and the failure stress of Verowhite was set as 64 MPa and the failure strain of TangoPlus was set as 0.6 according to pendulum impact test results.

A structural grid division and hexahedron element were adopted. The element characteristic size of the uniform brick-mud structure for  $k = 0$  was 0.40 mm. The element number and the number of nodes were 127261 and 252540, respectively. The element characteristic size of the gradient brick-mud structure for  $k = 0.0237$  was 0.32 mm, and the number of cells and the number of nodes were 262791 and 544700, respectively. When dividing the elements and selecting element size, the mean value of the quality factor of the elements should be greater than 0.8, so as to avoid the distortion caused by irregular elements and to ensure the validity of the results.

The hammer head and the support were simplified as rigid bodies (\*MAT\_RIGID). All degrees of freedom of the hammer head in the non-impact direction were constrained, and the supports were completely fixed. Node-to-surface tied constraint (\*CONTACT\_TIED\_NODES\_TO\_SURFACE) was adopted between the stiff and soft materials. It was assumed that the bonding interface of the soft and stiff materials has high enough strength, and the interface separation of the two materials is not considered. Furthermore, in order to avoid unexpected penetration, eroding single surface contact (\*CONTACT\_ERODING\_SINGLE\_SURFACE) was defined in areas where contact may occur.

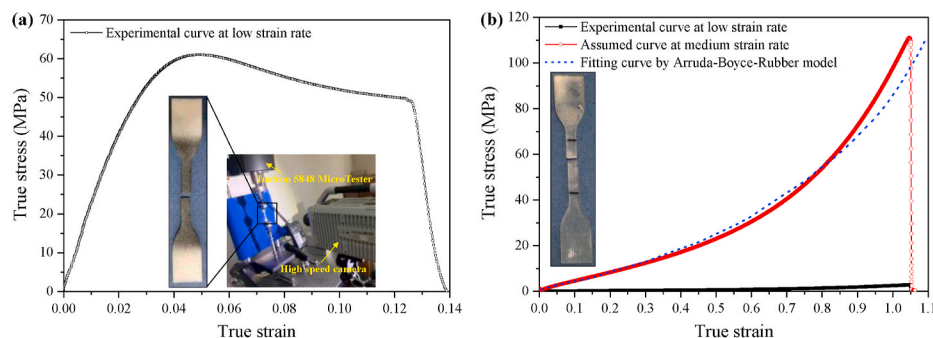


Fig. 4. True stress-strain curves. (a) Verowhite; (b) TangoPlus.

## 4. Results and discussion

### 4.1. Energy absorption and fracture characteristics of brick-mud structure

The experimental load-displacement curves and velocity-displacement curves of the hammer head were shown as solid symbols in Fig. 5. Immediately after the load acting on the sample reached the maximum, which called the maximum impact load point, the elements in the sample successively fail until the entirety breaks. The greater the cell size gradient is, the greater the maximum impact load and the displacement of the corresponding hammer are, and the higher the energy absorbed by the structure at the maximum impact load moment is. The energy absorbed by the structure in the impact process at this moment is used as an index to represent the impact resistance of the structure. For brick-mud sample with cell size gradient  $k = 0, 0.0237, 0.0301$  and  $0.0353$ , the absorbed energies obtained from the experimental data are  $0.50 \pm 0.05$  J,  $1.06 \pm 0.07$  J,  $1.77 \pm 0.06$  J and  $1.98 \pm 0.21$  J, respectively (Table 1). As can be seen, the energy absorbed by the structure in the impact process is effectively improved due to the gradient design of the cell size. The greater the cell size gradient is, the greater the energy absorption increase is. The energy absorption of the gradient brick-mud structure is up to 4 times that of the uniform brick-mud structure.

The hollow symbol in Fig. 5 represents the finite element simulation results of the brick-mud structure subjected to pendulum bob impact. The curves of the load and the velocity of the hammer head vs the displacement of the hammer head are almost the same as the experimental curves. Based on the numerical simulation curves, the energies absorbed by the uniform ( $k = 0$ ) and gradient ( $k = 0.0237$ ) brick-mud structures at the moment of maximum impact load were calculated to be  $0.53$  J and  $1.05$  J, respectively, with relative deviations from the experimental mean values were less than 6%, and they all fell in the range between the experimental mean values minus and plus the standard deviations. Therefore, the simulation result was well matched with the experimental result. The validity of the finite element modeling and the numerical simulation method in this paper was verified.

After the pendulum bob impact test, the crack propagation paths on the bottom and two side faces of the sample were photographed. Only one crack is formed in the bottom and the side faces of the uniform brick-mud structure, and the crack is nearly a straight line (Fig. 6(a)). The number of cracks in the bottom of the gradient structure is increased, and the crack propagation paths on the bottom and the side faces are zigzag (Fig. 6(b)–(d)). When the cell size gradient is relatively small, only one obvious crack is formed in the bottom of the structure and is accompanied by a local micro-crack. As the gradient is increased, multiple intersecting cracks are generated in the bottom of the structure, and multiple small blocks appear in a fracture area of the sample. Specifically, when the cell size gradient is increased, the number of cracks in the bottom is increased, the crack deflection degree is increased, and the expansion path is more zigzag. Therefore, a greater fracture area is

**Table 1**

Absorbed energy and strain energy of the brick-mud structure at the maximum impact load moment.

Cell size gradient $k$	Absorbed energy (J)		Strain energy (J)	Ratio of strain energy to absorbed energy
	Experiment	Simulation	Simulation	
0	$0.50 \pm 0.05$	0.53	0.49	92.5%
0.0237	$1.06 \pm 0.07$	1.05	0.94	90.0%

achieved, and the energy absorption of the structure in the impact process is improved.

### 4.2. Strain energy analysis

In the impact process, the energy absorbed by the structure is mainly stored in the form of strain energy. Fig. 7(a) shows a change curve of strain energy stored in the brick-mud structure with the displacement of the hammer head. Before any element failure, as the displacement of the hammer head is increased, the strain energy stored in both structures is gradually increased. For the uniform brick-mud structure and the gradient brick-mud structure, the displacements of the hammer head at the maximum impact load moment are  $1.24$  mm and  $1.83$  mm, respectively, while the stored strain energy is  $0.49$  J and  $0.94$  J, respectively, and accounts for about 92.5% and 90.0% of the energy absorbed by the structure, respectively (Table 1). When the displacement of the hammer head is  $1.24$  mm, the strain energy stored in the two structures is approximately equal. The uniform structure is about to fail at this moment, and its strain energy stored reaches the maximum. In contrast, the gradient structure does not fail, the strain energy stored in the structure continues to rise until the displacement of the hammer head is  $1.83$  mm. At this moment, the gradient structure is about to fail, and the strain energy reaches the maximum.

The strain energy of the hammer head stored in the structure and the displacement at any moment were divided by the maximum strain energy stored in the structure and the maximum displacement of the hammer head, respectively, to obtain the non-dimensional curves of the total strain energy vs the displacement of the hammer head (Fig. 7(b)). Obviously, the dimensionless total strain energy vs hammer head displacement curves of the uniform and gradient brick-mud structures are almost consistent. Similarly, the strain energy stored in a given area of the stiff material, and the soft material are collected and then non-dimensionalized. The resulting dimensionless curves of the two structures are also nearly identical. Therefore, the dimensionless strain energy-hammer head displacement curve represents the common rules of changes of the strain energy stored in the brick-mud structure in the pendulum impact process.

Fig. 8 shows the percentage of the strain energy stored in the soft and stiff materials to the total strain energy at the maximum impact load moment. The stiff material in the sample is only located in the brick-mud

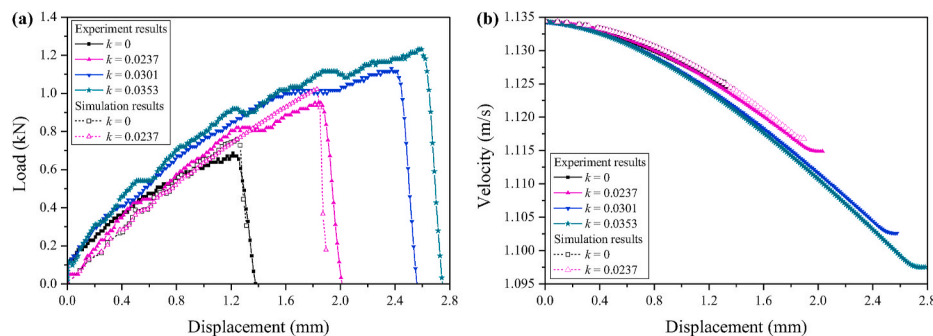
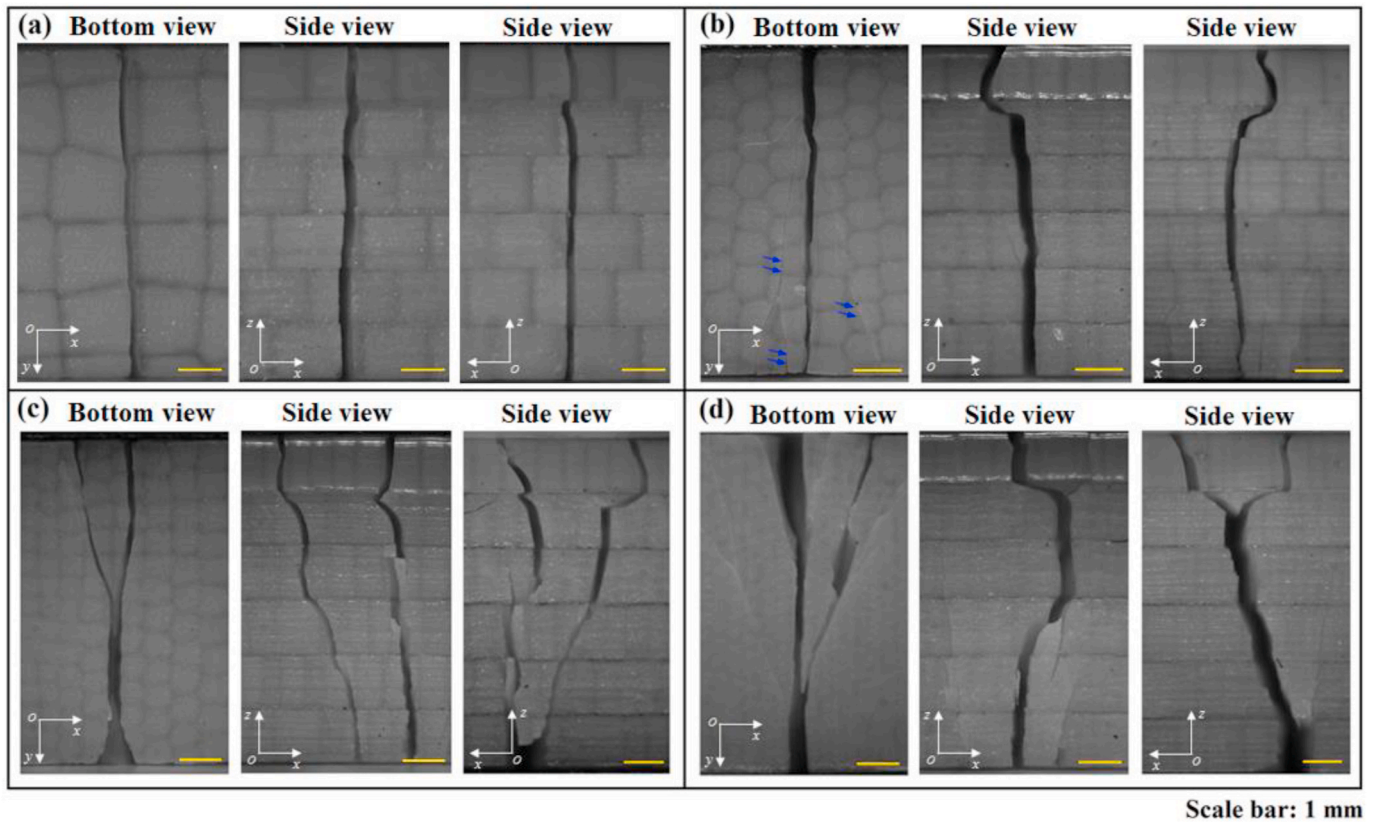


**Fig. 5.** Pendulum impact experiment and numerical simulation results of brick-mud structures. The change curves of (a) load-displacement of hammer head, (b) velocity-displacement of hammer head. The impact velocity of hammer head is  $1.1344$  m/s.



Scale bar: 1 mm

Fig. 6. Crack propagation paths of brick-mud structures after pendulum impact test. The cell size gradient  $k$  = (a) 0; (b) 0.0237; (c) 0.0301; (d) 0.0351.

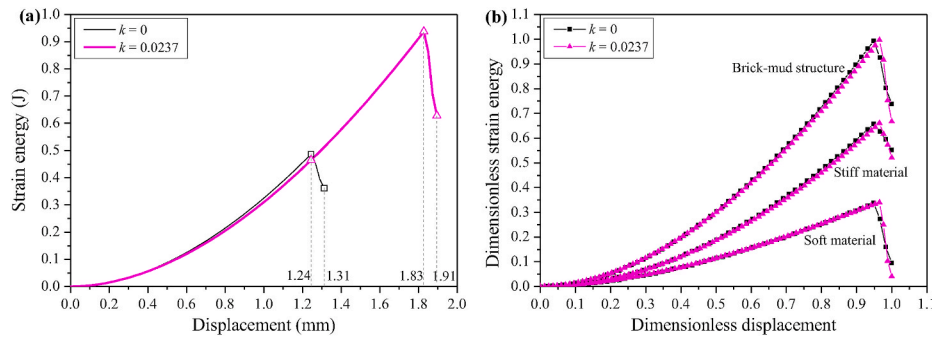


Fig. 7. Strain energy stored in the brick-mud structure versus displacement of the hammer head. (a) Actual curves; (b) Dimensionless curves.

structure layer, its volume fraction is 77%, and the strain energy stored therein accounts for 66% of the total strain energy. When the structure is subjected to vertical impact and generates bending deformation, the strain energy stored in the stiff material is mainly contributed by the horizontal normal stress  $\sigma_{xx}$ , horizontal normal strain  $\epsilon_{xx}$  (Fig. 9(a) and (b)), vertical normal stress  $\sigma_{zz}$  and vertical normal strain  $\epsilon_{zz}$  (Fig. 9(c) and (d)). The  $\sigma_{xx}$  and  $\epsilon_{xx}$  in the brick-mud structure farther from the neutral layer is higher, and the  $\sigma_{zz}$  and  $\epsilon_{zz}$  in the brick-mud structure in contact with the hammer head is higher than those of the other layers. Therefore, the strain energy of the stiff material in the 1st and 6th brick-mud structure layers is the largest, accounting for about 20% of the total strain energy; the strain energy in the 2nd and 5th layers is the second largest, accounting for about 9%; and the strain energy in the 3rd and 4th layers is the smallest, accounting for about 5%.

The soft materials in the sample are distributed between and within the brick-mud structure layers, the volume fraction is 23%, and the stored strain energy accounts for 34% of the total strain energy. On the one hand, the volume fraction of the interlayer soft material is only 6%,

while the strain energy stored therein accounts for 31% of the total strain energy. When the structure generates bending deformation, relative sliding along the lengthwise direction between the layers of the brick-mud structure will cause higher shear stress  $\sigma_{xz}$  and shear strain  $\epsilon_{xz}$  of the interlayer soft material (Fig. 10(a) and (b)). In addition, in a local area close to the hammer head and the supporting end, the vertical pressure stress  $\sigma_{zz}$  in the structure is relatively high (Fig. 10(c)), which will limit the relative sliding of the brick-mud structure layer, resulting in greater  $\sigma_{xz}$  and  $\epsilon_{xz}$  of the interlayer soft material closer to the neutral layer. The strain energy stored in the interlayer soft material is mainly the contribution of  $\sigma_{xz}$  and  $\epsilon_{xz}$ . The closer it gets to the neutral layer, the higher the strain energy is. The strain energy of the 3rd layer is the largest, accounting for about 9% of the total strain energy; the strain energy in the 2nd and 4th layers is the second largest, accounting for about 8%; and the strain energy in the 1st and 5th layers is the smallest, accounting for about 4%. On the other hand, the volume fraction of the soft material in the brick-mud layer is 17%, which is about 2.8 times the volume fraction of the interlayer soft material, but the strain energy



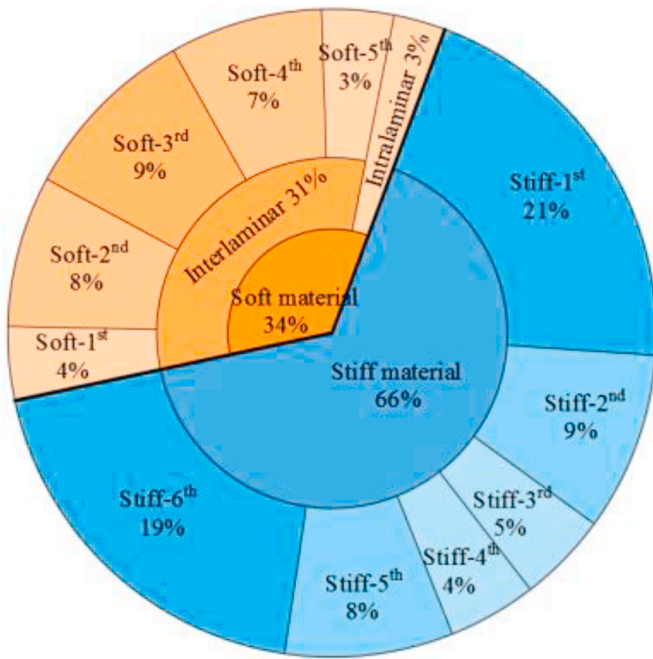


Fig. 8. Percentage of the strain energy stored in the soft and stiff materials to total strain energy at the maximum impact load moment.

stored therein is only 1/10 of that of the interlayer soft material, which is almost negligible.

Moreover, the sum of strain energy stored in each column of cells was calculated based on the strain energy density distribution of the 1st and 6th brick-mud structure layers (Fig. 11(a) and (b)), then the sum was divided by the sum of the volumes of the column of cells to obtain the distribution of the equivalent strain energy density of the column of cells along the lengthwise direction of the sample (Fig. 11(c)). A high strain energy density area is located at the middle of the sample, and the smaller the distance from the symmetry axis of the sample is, the higher the strain energy density is. At the same displacement 1.24 mm of the hammer head, the strain energy density distribution curves of the uniform and gradient structures are almost consistent, and the strain energy stored in the two structures is almost equal. After that, elements in the uniform structure begin to fail, while the strain energy density at various points in the gradient structure continues to increase until the displacement of the hammer head reaches 1.83 mm. The strain energy density of the gradient structure is higher than that of the uniform structure at the same position and at the maximum impact load moment. The smaller the distance from the symmetry axis of the sample is, the greater the difference value of strain energy density between the gradient and uniform structures is. At the middle of the sample, the maximum strain energy density of the gradient structure is 2.1 times that of the uniform structure. Therefore, due to the gradient design of the cell size along the lengthwise direction of the sample, the stress and strain of the structure in the impact process are redistributed in such a way that, the strain energy density of various points in the sample,

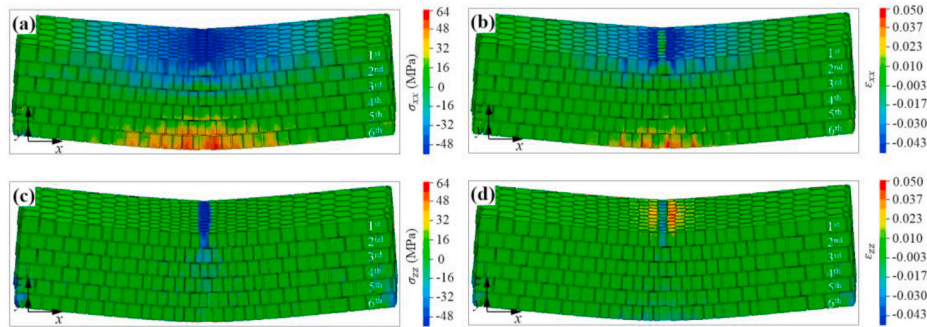


Fig. 9. (a) Horizontal normal stress, (b) horizontal normal strain, (c) vertical normal stress, and (d) vertical normal strain of the stiff material in the span area at the maximum impact load moment.

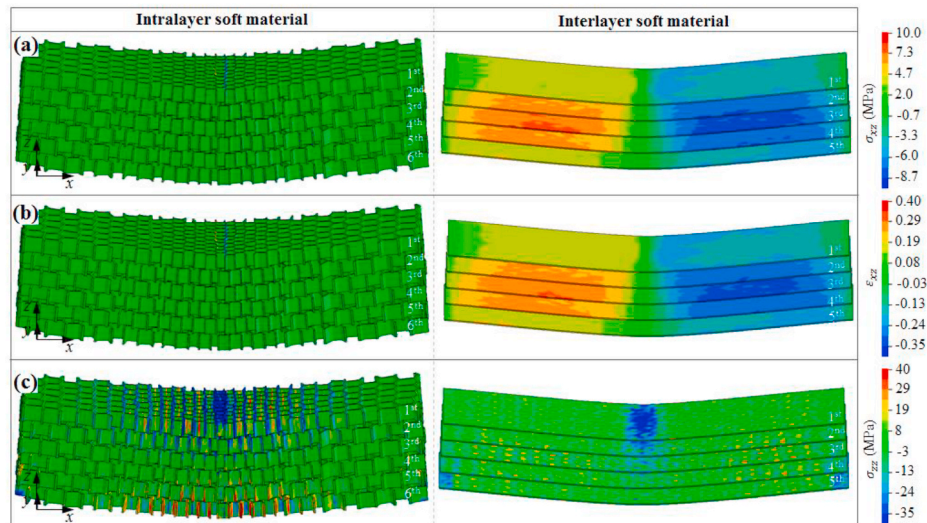
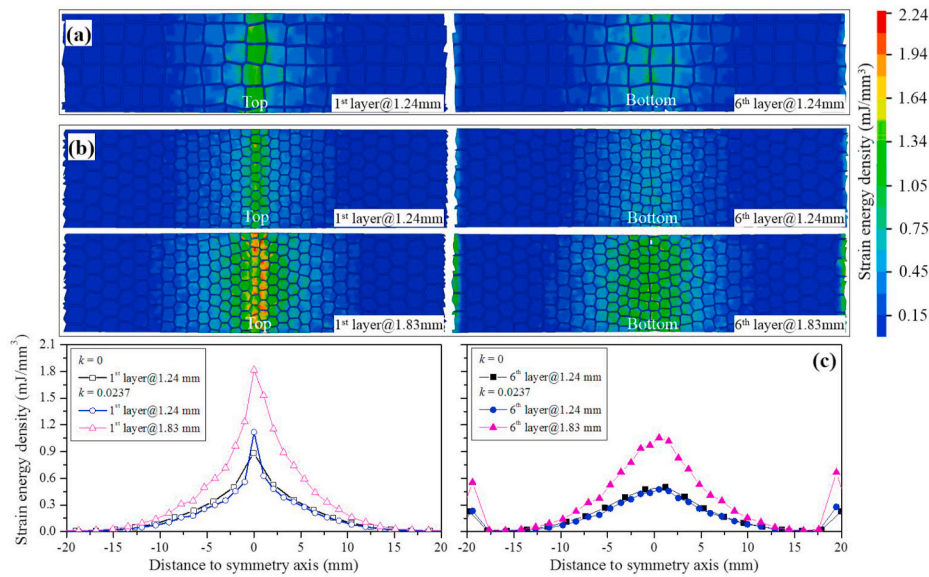


Fig. 10. (a) Shear stress and (b) shear strain in  $xz$  plane, (c) vertical normal stress of the soft materials in the span area at the maximum impact load moment.



**Fig. 11.** Strain energy density of brick-mud structures in the span area. Strain energy density contours of brick-mud structures with cell size gradient  $k =$  (a) 0 and (b) 0.0237, respectively; (c) Distribution of the equivalent strain energy density of the column of cells along the lengthwise direction of the sample.

particularly the middle area of the sample, is increased. Thus, the energy absorbed by the gradient structure in the impact process is much higher than that of the uniform structure.

#### 4.3. Failure mechanism analysis

Fig. 12 shows the distribution contour of the first principal stress in the span area of the brick-mud structure. The cell at the middle of the bottom surface of the structure has the highest stress and fails first. The crack paths and positions on the bottom surface and side faces of the structure are approximate to the experimental results, the uniform structure has only one nearly straight crack (Fig. 12(a)), while the main crack on the bottom surface of the gradient structure accompanied by local micro-cracks and side face cracks presents zigzag deflection

(Fig. 12(b)).

In a 40 mm span area, a layer of elements on the bottommost surface of the sample was divided into 53 and 10 equal parts along the lengthwise direction and the widthwise direction of the sample, respectively, and the maximum value of the first principal stress of all elements in each equal segment was counted to obtain the distribution of the maximum first principal stress on the bottom surface of the brick-mud structure (Fig. 13). Upon reaching the maximum impact load of the uniform structure, the displacement of the hammer head is 1.24 mm, the stress is unevenly distributed along the widthwise direction of the sample, and the change amplitude is 10.6 MPa (solid symbols in Fig. 13 (a)); and there are local fluctuations in the middle area along the lengthwise direction, and the change amplitude is 7.9 MPa (solid symbols in Fig. 13(b)).

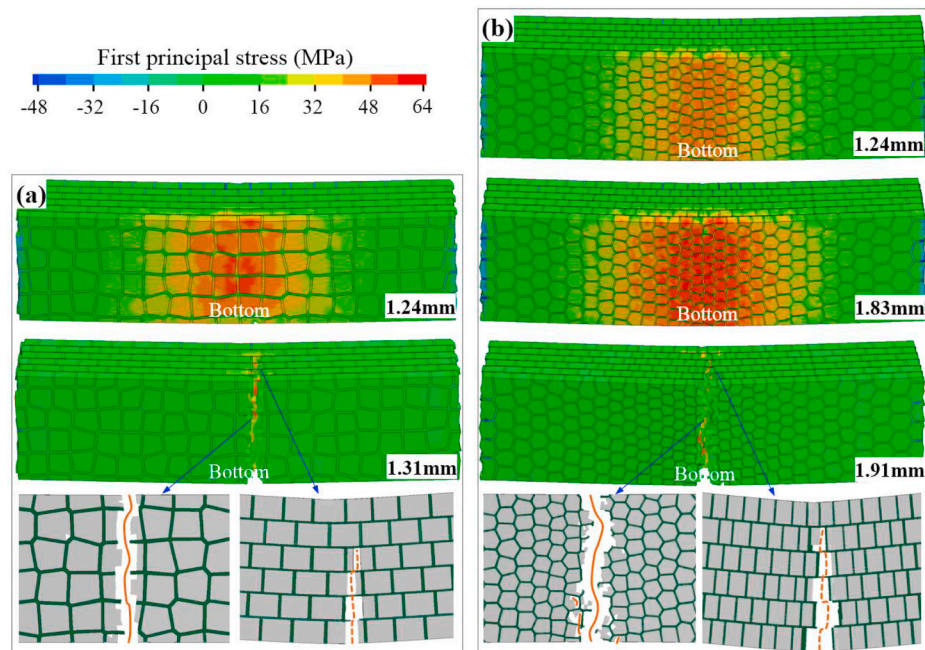


**Fig. 12.** The first principal stress distribution of the brick-mud structure in the span area. The cell size gradient  $k =$  (a) 0; (b) 0.0237, respectively.

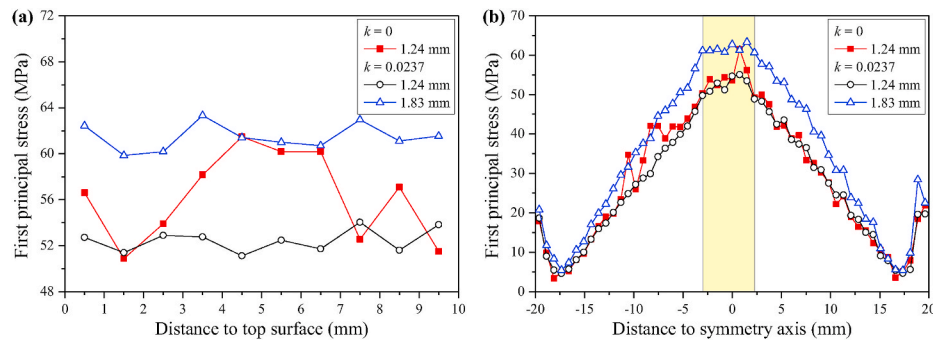


**Fig. 13.** Distribution of the maximum first principal stress on the bottom surface of the brick-mud structure along the (a) widthwise and (b) lengthwise direction of the sample.

Compared with the uniform structure, the first principal stress distribution along the widthwise direction of the gradient structure is more uniform. When the displacement of the hammer head is 1.24 mm, the change amplitude is only 2.9 MPa, and the maximum value is 7.4 MPa lower than that of the uniform structure. Therefore, the uniform structure is closer to the failure stress and is prone to failure. The two structures at the moment prior to failure were compared. The change amplitude of the stress of the gradient structure is 3.5 MPa, which is still relatively small, and the maximum stress is 63.6 MPa, while the maximum stress of the uniform structure is 61.8 MPa. At next moment, the maximum stresses in the two structures are both increased to 64 MPa and element failures occur. Obviously, the increase in the stress of the gradient structure in the same analysis time step is smaller (hollow symbols in Fig. 13(a)), compared with the uniform structure. In addition, the stress distribution curve of the gradient structure along the lengthwise direction is relatively smooth, and when the displacement of the hammer head is 1.83 mm, the central area of  $-3.0$ – $2.3$  mm appears a straight line, indicating the stress distribution in this area is uniform (hollow symbols in Fig. 13(b)).

When the stress distribution is not uniform, a high-stress element will exceed the failure stress earlier than other elements, and the possibility of fracture is increased. When the displacement of the hammer head is 1.24 mm, the two structures have the same bending deformation, but the uniform structure is easy to form an area with excessive stress due to the large middle cell size and poor deformation coordination ability (Fig. 12(a)). In contrast, the stress distribution of the gradient structure is improved, this is because the middle cell size is small. The same bending deformation is dispersed by more cells, and thus the deformation coordination ability is better. And the overall structure bears more bending deformation before fracture, thus having greater strain energy (Fig. 12(b)).

## 5. Conclusions

Based on the brick-mud microstructure of natural nacre, a novel structure with cell size changing in a gradient mode was proposed and prepared. Combined with the pendulum impact tests and finite element analysis, the failure process and mechanism of the gradient brick-mud structure under impact were studied. Results show that due to the gradient design of cell size perpendicular to the impact direction, the stress and strain distribution of the structure are improved, and the strain energy density of various points in the sample, particularly the middle area of the sample, is increased. Thus, the energy absorbed by the gradient structure in the impact process is much higher than that of the uniform structure. Moreover, the larger the cell size gradient is, the more the energy absorbed by the structure during the impact process. The energy absorption of the gradient brick-mud structure is up to 4 times that of the uniform brick-mud structure.

General laws of strain energy stored in the stiff and soft materials in brick-mud structures at the moment of maximum impact load were

further investigated. Under the premise of the same parameters such as the volume fraction of the stiff material, the thickness of brick-mud structure layer, etc., the increase of cell size gradient can improve the total strain energy stored in the gradient structure, but it has no effect on the percentage of strain energy stored in the stiff or soft material. Due to the coordinated deformation of brick-mud structures, the stiff material generates higher horizontal and vertical normal stresses and normal strains. The strain energy stored in the stiff material accounts for 66% of the total strain energy stored in the gradient structure, which is about 2 times that of the soft material. In addition, due to the relative sliding between the brick-mud structure layers, the interlayer soft material produces higher shear stress and shear strain. Therefore, accounting for only 1/3 volume of the intralayer soft materials, the strain energy stored in the interlayer soft material reaches 10 times that of the intralayer soft material.

## Author statement

X.H. Xu made substantial contributions to the conception or design of the work, and helped drafted and revised it critically for important content.

Z.Q. Wei conducted all simulations and performed the analysis of data for the work.

All persons who have made substantial contributions to the work have been named in the manuscript and approved the final version to be published.

We agree to be accountable for all aspects of the work in ensuring that questions related to the accuracy or integrity of any part of the work are appropriately investigated and resolved.

## Declaration of competing interest

The authors declare that they have no known competing financial interests or personal relationships that could have appeared to influence the work reported in this paper.

## Acknowledgments

The authors gratefully acknowledge the support provided by the National Natural Science Foundation of China (No. 11672297), the Strategic Priority Research Program of the Chinese Academy of Sciences (No. XDB22020200).

## References

- [1] Ha NS, Lu GX. A review of recent research on bio-inspired structures and materials for energy absorption applications. *Compos B Eng* 2020;181:107406.
- [2] Ghazlan A, Ngo TD, Tan P, Xie YM, Tran P, Donough M. Inspiration from Nature's body armours – a review of biological and bioinspired composites. *Compos B Eng* 2021;205:108513.



- [3] Bouville F, Maire E, Meille S, Van de Moortele B, Stevenson AJ, Deville S. Strong, tough and stiff bioinspired ceramics from brittle constituents. *Nat Mater* 2014;13(5):508–14.
- [4] Miranda P, Pajares A, Meyers MA. Bioinspired composite segmented armour: numerical simulations. *J Mater Res Technol* 2019;8(1):1274–87.
- [5] Naleway SE, Porter MM, McKittrick J, Meyers MA. Structural design elements in biological materials: application to bioinspiration. *Adv Mater* 2015;27(37):5455–76.
- [6] Yaraghi NA, Kisailus D. Biomimetic structural materials: inspiration from design and assembly. *Annu Rev Phys Chem* 2018;69:23–57.
- [7] Espinosa HD, Rim JE, Barthelat F, Buehler MJ. Merger of structure and material in nacre and bone - perspectives on de novo biomimetic materials. *Prog Mater Sci* 2009;54(8):1059–100.
- [8] Ko K, Jin S, Lee SE, Hong JW. Impact resistance of nacre-like composites diversely patterned by 3D printing. *Compos Struct* 2020;238:111951.
- [9] Flores-Johnson EA, Shen LM, Guiamatsia I, Nguyen GD. Numerical investigation of the impact behaviour of bioinspired nacre-like aluminium composite plates. *Compos Sci Technol* 2014;96:13–22.
- [10] Tran P, Ngo TD, Ghazlan A, Hui D. Bimaterial 3D printing and numerical analysis of bio-inspired composite structures under in-plane and transverse loadings. *Compos B Eng* 2017;108:210–23.
- [11] Ghazlan A, Ngo T, Le TV, Nguyen T, Remennikov A. Blast performance of a biomimetic panel based on the structure of nacre – a numerical study. *Compos Struct* 2020;234:111691.
- [12] Gu GX, Takaffoli M, Hsieh AJ, Buehler MJ. Biomimetic additive manufactured polymer composites for improved impact resistance. *Extreme Mech Lett* 2016;9:317–23.
- [13] Jia ZA, Yu Y, Hou SY, Wang LF. Biomimetic architected materials with improved dynamic performance. *J Mech Phys Solid* 2019;125:178–97.
- [14] Grunenfelter LK, Suksangpanya N, Salinas C, Milliron G, Yaraghi N, Herrera S, Evans-Lutterodt K, Nutt SR, Zavattieri P, Kisailus D. Bio-inspired impact-resistant composites. *Acta Biomater* 2014;10(9):3997–4008.
- [15] Gu GX, Takaffoli M, Buehler MJ. Hierarchically enhanced impact resistance of bioinspired composites. *Adv Mater* 2017;29(28).
- [16] Jiang HY, Ren YR, Liu ZH, Zhang SJ, Lin ZQ. Low-velocity impact resistance behaviors of bio-inspired helicoidal composite laminates with non-linear rotation angle based layups. *Compos Struct* 2019;214:463–75.
- [17] Weaver JC, Milliron GW, Miserez A, Evans-Lutterodt K, Herrera S, Gallana I, et al. The stomatopod dactyl club: a formidable damage-tolerant biological hammer. *Science* 2012;336(6086):1275–80.
- [18] Wu KJ, Zheng ZJ, Zhang SS, He LH, Yao HB, Gong XL, et al. Interfacial strength-controlled energy dissipation mechanism and optimization in impact-resistant nacreous structure. *Mater Des* 2018;163:107532.
- [19] Wu XD, Meng XS, Zhang HG. An experimental investigation of the dynamic fracture behavior of 3D printed nacre-like composites. *J Mech Behav Biomed* 2020;112:104068.
- [20] Ritchie RO. The conflicts between strength and toughness. *Nat Mater* 2011;10:817–22.
- [21] Xu LR, Rosakis AJ. Impact failure characteristics in sandwich structures Part II: effects of impact speed and interfacial strength. *Int J Solid Struct* 2002;39(16):4237–48.
- [22] Liu ZQ, Meyer MA, Zhang ZF, Ritchie RO. Functional gradients and heterogeneities in biological materials: design principles, functions, and bioinspired applications. *Prog Mater Sci* 2017;88:467–98.
- [23] Habibi MK, Samaei AT, Gheshlaghi B, Lu J, Lu Y. Asymmetric flexural behavior from bamboo's functionally graded hierarchical structure: underlying mechanisms. *Acta Biomater* 2015;16:178–86.
- [24] Gu Y, Xu XH. Novel gradient design and simulation of Voronoi structures. *Int J Appl Mech* 2018;10(7):1850079.
- [25] Liang MZ, Li ZB, Lu FY, Li XY. Theoretical and numerical investigation of blast responses of continuous-density graded cellular materials. *Compos Struct* 2017;164:170–9.
- [26] Lin Y, Yu Q, Pan J, Duan FH, Ritchie RO, Li Y. On the impact toughness of gradient-structured metals. *Acta Mater* 2020;193:125–37.
- [27] Moering J, Ma XL, Malkin J, Yang MX, Zhu YT, Mathaudhu S. Synergetic strengthening far beyond rule of mixtures in gradient structured aluminum rod. *Scripta Mater* 2016;122:106–9.
- [28] Brostow W, Castaño VM. Voronoi polyhedra as a tool for dealing with spatial structures of amorphous solids, liquids and gases. *J Mater Educ* 1999;21:297–304.
- [29] Brostow W, Hagg Lobland HE. Materials: introduction and applications. John Wiley & Sons; 2017.
- [30] Zhu YJ, Ding WF, Yu TY, Xu JH, Fu YC, Su HH. Investigation on stress distribution and wear behavior of brazed polycrystalline cubic boron nitride superabrasive grains: numerical simulation and experimental study. *Wear* 2017;376:1234–44.
- [31] Ko K, Jin S, Lee SE, Lee I, Hong JW. Bio-inspired bimaterial composites patterned using three-dimensional printing. *Compos B Eng* 2019;165:594–603.
- [32] PolyJet materials data sheet. USA: Stratasys; 2016.
- [33] Rohbeck N, Ramachandramoorthy R, Casari D, Schurch P, Edwards TEJ, Schilinsky L, Philippe L, Schwiedrzik J, Michler J. Effect of high strain rates and temperature on the micromechanical properties of 3D-printed polymer structures made by two-photon lithography. *Mater Des* 2020;195:108977.
- [34] Sherwood JA, Frost CC. Constitutive modeling and simulation of energy absorbing polyurethane foam under impact loading. *Polym Eng Sci* 1992;32:1138–46.
- [35] LS-DYNA® Keyword. User's manual. Livemore. California, USA: Livemore Software Technology Corporation; 2007.